Reaction Kinetics, Mechanisms and Catalysis (2024) 137:913–934
https://doi.org/10.1007/s11144-024-02581-6

Cu–Mn–Al based catalyst for the direct syngas to dimethyl ether conversion

Humberto Blanco[1,3] · Luz A. Palacio[2] · Victor Rodrigues[1] · Arnaldo Faro Jr.[1]

Received: 22 December 2023 / Accepted: 21 January 2024 / Published online: 20 February 2024

Abstract

Cu–Mn–Al mixed oxides were prepared by calcination of carbonate layered double hydroxides. Four materials were prepared with nominal Cu/Mn ratios in the 0.5–2.0 range and 0.19 nominal Al atom fraction relative to metal ions. Reduction of the oxide precursors was followed by in situ X-ray absorption and X-ray diffraction and showed that copper was totally reduced, and manganese reduced mainly to Mn^{2+}. Copper metal surface area by N_2O decomposition after in situ reduction showed that the dispersion increased with decreasing copper content in Mn–Cu–Al catalysts. In methanol synthesis from syngas, the methanol productivity and selectivity achieved values up to 35 mol kg^{-1} h^{-1} and 94% with Cu–Mn–Al catalysts. In the direct syngas to DME reaction, using γ-alumina as the methanol dehydration component, the productivity of the Cu–Mn–Al catalyst with 0.5 Cu/Mn ratio stood-out from that of the remaining catalysts.

Keywords Cu–Mn–Al · Cu–Zn–Al · X-ray absorption · Methanol synthesis · Direct syngas to dimethyl ether conversion

Retired: Arnaldo Faro.

✉ Arnaldo Faro Jr.
farojr@gmail.com

[1] Laboratório de Catálise Heterogênea, Instituto de Química, Universidade Federal do Rio de Janeiro, Av. Athos da Silveira Ramos, 149–302/A, Rio de Janeiro, RJ CEP: 21941-909, Brazil

[2] Instituto de Química, Universidade do Estado de Rio de Janeiro, Rua São Francisco Xavier, 524, Rio de Janeiro, RJ CEP: 20550-900, Brazil

[3] Instituto Colombiano del Petróleo, Ecopetrol, Piedecuesta código postal 681011, Santander, Colombia

Introduction

There is a universally growing pressure for the replacement of fuels derived from petroleum or coal, by environmentally friendlier ones. Among these, stand-out fuels derived from natural gas and from biomass. The most widespread method for doing this is via the intermediate production of synthesis gas (syngas), the so-called reforming processes, that may be applied to most carbon-containing raw materials [1–3]. Syngas is a mixture of hydrogen and carbon monoxide, generally containing a minor amount of carbon dioxide, that can be converted to hydrocarbon fuels, olefins or alcohols by means of the Fischer–Tropsch process [3] or to methanol via carbon monoxide and carbon dioxide hydrogenation [4, 5].

Methanol may be directly used as a clean fuel in combustion engines [6] and in fuel cells [7], may be transformed into gasoline by the so-called MTG [8] process or it may be converted to dimethyl ether (DME) [9]. The latter is an important chemical, used as a non-CFC aerosol propellant, solvent and refrigerating fluid [10]. However, its main interest nowadays is as an environmentally friendly alternative to fossil fuels. It has physical properties similar to those of propane, which makes it suitable for replacing or to be added to liquefied petroleum gas (LPG) [10]. It also has a cetane rating somewhat higher than that of diesel fuel and of course burns without emission of particulates or sulfur oxides [11]. Therefore, DME can be used as an environmentally friendlier alternative to diesel.

DME is traditionally obtained indirectly from syngas in a two-step process by methanol dehydration [12, 13]. There is a growing interest however in DME production in a one-step process directly from syngas [14, 15]. The reactions involved are the following ones in both process concepts [16]:

$$CO(g) + 2H_2(g) \rightleftharpoons CH_3OH(g) \quad \Delta_r H^0_{298} = -90\,\text{kJ mol}^{-1} \tag{1}$$

$$CO_2(g) + 3H_2(g) \rightleftharpoons CH_3OH(g) + H_2O(g) \quad \Delta_r H^0_{298} = -49.5\,\text{kJ mol}^{-1} \tag{2}$$

$$2CH_3OH(g) \rightleftharpoons \left(CH_3\right)_2O(g) + H_2O(g) \quad \Delta_r H^0_{298} = -23.4\,\text{kJ mol}^{-1} \tag{3}$$

$$H_2O(g) + CO(g) \rightleftharpoons H_2(g) + CO_2(g) \quad \Delta_r H^0_{298} = -41.2\,\text{kJ mol}^{-1} \tag{4}$$

As water is produced in reaction 3 and consumed in the water-gas shift reaction 4, when both methanol synthesis and dehydration are conducted in the same reactor the overall carbon monoxide hydrogenation reaction is described by Eq. 5 [16].

$$3CO(g) + 3H_2(g) \rightleftharpoons \left(CH_3\right)_2O(g) + CO_2(g)\Delta_r H^0_{298} = -245.8\,\text{kJ mol}^{-1} \tag{5}$$

In the two-stage process, methanol and thus the subsequent DME productivity, are limited by the methanol synthesis equilibrium [17] (reaction 1). In the one stage process, the overall reaction is reaction 5, whose equilibrium conversion is much higher than that of reaction 1 [15, 16]. Therefore, in the direct process, the maximum DME yield is much less limited by thermodynamics. From the kinetic standpoint, it is

generally considered that methanol production in the synthesis reaction occurs mainly from carbon dioxide [18, 19], rather than from carbon monoxide hydrogenation. In the two-step process, the coupling of the methanol dehydration reaction 3 with the water gas shift reaction (WGSR) keeps a high carbon dioxide concentration, which is favorable to the reaction kinetics [20].

The one-step syngas to DME process (STD process) must employ, either a bi-functional methanol synthesis/methanol dehydration catalyst [14, 21] or a mixture of catalysts for these functions [21–23]. The methanol dehydration component is a catalyst with surface acidic properties, such as a zeolite or γ-alumina. The most common methanol synthesis catalyst is a Cu–Zn–Al oxide [24, 25], which is also active in WGSR [26, 27]. This oxide and γ-alumina can perform their functions under the same conditions, so their mixture is an efficient catalyst system for the one-step syngas to DME process [21, 23].

Improvements in the STD process may be sought by investigating new promising catalysts, either for the methanol synthesis component or for methanol dehydration component of the mixed catalyst system. In previous work [28, 29] we have shown that improvements in the STD reaction are obtained by using alumina-supported niobia instead of the conventional γ-alumina as the methanol dehydration component in a mixed catalyst system with the conventional Cu–Zn–Al catalyst. In the present work we focus on the performance of Cu–Mn–Al catalysts prepared from ternary hydrotalcite-like precursors as the hydrogenation component in a mixed catalyst system for the direct syngas to DME conversion. In a former paper, we have shown [17] that a Cu–Mn–Al catalysts obtained by calcination of a carbonate layered double hydroxide (LDH), after hydrogen reduction performed better than an industrial Cu–Zn–Al catalyst in methanol synthesis from syngas in the liquid phase. Furthermore, the CuMn system is known to be active in the water-gas shift reaction [30, 31] (reaction 4 above), that plays a very important role in the STD reaction cycle. Therefore, the proposed catalyst system is promising for the STD reaction.

There is scarce information in the open literature about Cu–Mn–Al catalysts for DME synthesis. A 2001 paper by Qi et al. [32], reported on the performance of alumina-supported Cu–Mn catalysts, on syngas to DME conversion, without combination with a dehydration catalyst. Synergy between copper and manganese was observed, but no comparison with the traditional Cu–Zn–Al system and little characterization of the materials was provided. In two other papers, manganese was used as an additive to Cu–Zn–Al with positive results [33, 34].

In the present paper, the Cu/Mn ratio was varied over a large range and the effects of this parameter on the physicochemical and catalytic properties of the materials were studied. The catalysts that performed better in methanol synthesis were used as the methanol synthesis component together with a γ-alumina as the methanol dehydration component in the STD reaction.

Experimental

Catalyst preparation

LDH precursors were prepared by the addition of two solutions to a beaker previously filled with 200 mL of deionized water, at a constant temperature of 338 K. The first was an acidic solution composed of the metal nitrates ($Al(NO_3)_3{\cdot}9H_2O$, $Cu(NO_3)_2{\cdot}3H_2O$, $Mn(NO_3)_2{\cdot}4H_2O$, $Zn(NO_3)_2{\cdot}6H_2O$) in relative concentrations adequate to produce the materials according to the targeted metal molar fractions, but with constant total concentration equal to 0.4 M. The second was a basic solution containing ammonium carbonate (0.05 M) and ammonium hydroxide (0.7 M). The pH of the reaction mixture was varied between 6.5 and 8.0, in a controlled fashion, by means of a pH controller that allowed the alternate addition of the nitrates solution to lower the pH and of the ammoniacal solution to raise the pH. After aging of the suspension for 18 h, filtration and drying, the precipitates were calcined at 673 K to obtain the mixed oxides.

Four ternary catalysts were prepared with nominal molar Cu:Mn ratios equal to 0.2, 0.5, 1.0 and 2.0, and nominal 0.19 molar ratio of Al to total metal elements in all materials. The adopted nomenclature for the LDH precursors was CuMnYAl, where Y represents the nominal Cu:Mn molar ratio. For the calcined materials letter C is added to the same naming scheme, and for the reduced catalysts, letter R is used instead of C.

For comparison with the conventional catalyst, a Cu–Zn–Al material was prepared by the same method, with a 2.0 Cu:Zn ratio and a 0.16 nominal molar ratio of Al to total metal elements. An industrial Cu–Zn–Al methanol synthesis catalyst (named CMSC) was made available by PROSINT Química S.A. (Brazil).

Characterization

The characterization methods used here were described in full detail in our previous work [17]. The LDH precursors were characterized by powder X-ray diffraction (XRD). The oxides were characterized by nitrogen physisorption for determination of surface areas using the BET method, by inductively coupled plasma optical emission spectroscopy (ICP-OES) and by XRD.

Reduced materials were characterized, during in situ reduction under a 5% H_2 in He mixture, by X-ray absorption near-edge spectroscopy (XANES), by extended X-ray absorption fine structure spectroscopy (EXAFS) at the Cu K- and Mn K-edges and by XRD at the Laboratório Nacional de Luz Síncrotron, Campinas, Brazil. The copper dispersion was estimated from N_2O decomposition on the metal surface generated after reduction up to 538 K during a temperature-programmed reduction (TPR) experiment, followed by a second TPR for titration of the oxygen deposited on the copper surface.

Catalytic tests

Catalytic evaluation was performed with all catalysts in methanol synthesis and with selected ones in the direct syngas to DME (STD) reaction. The measurements were carried-out in a continuous stirred tank reactor (CSTR). The powdered catalyst charge (0.2–0.28 g) was such that the copper mass in the reactor was always the same. The suspension medium for the catalyst powder was *n*-hexadecane. The catalysts were activated in situ employing pure hydrogen at 50 bar, 538 K for 18 h. Subsequently, the reaction was started by replacing the reducing gas by the synthesis gas (H_2/CO = 2 mole basis, 170 mL min^{-1}). Each test lasted for 8 h, during which the reactor effluent was periodically sampled to an online gas chromatograph. Further details may be found in our previous publication [17].

The procedure in the STD reaction was the same, the only difference being that a Pural SB γ-alumina also in powder form (granulometry between 44 and 88 μm) previously calcined at 823 K for 4 h, was added to the methanol synthesis catalyst as the methanol dehydration component. The alumina amount was chosen so that the molar Cu/Al ratio was 0.41 in all experiments, considering the copper and aluminium contents of each catalyst. Therefore, masses between 0.2 and 0.3 g were used for Cu containing catalyst and between 0.28 and 0.4 g for γ-alumina.

Carbon monoxide conversions were calculated from the expression shown in Eq. 6.

$$X = \frac{\sum_p n_p \times A_p \times f_p}{\sum_t n_t \times A_t \times f_t} \times 100 \tag{6}$$

where X (dimensionless) is the percent conversion, subscripts p and t represent carbon-containing products and all carbon-containing substances, n is number of carbon atoms in each substance (2 for DME and 1 for all others), A_i is the chromatographic area of the peak corresponding to substance i and f_i is the chromatographic sensitivity factor.

Percent selectivity S_i to substance i (dimensionless) was calculated from Eq. 7.

$$S_i = \frac{n_i \times A_i \times f_i}{\sum_p n_p \times A_p \times f_p} \times 100 \tag{7}$$

Here the symbols n, A and f have the same meaning as in Eq. 1. Subscript i indicate a given product.

Productivities P_i for a given product i (mol kg^{-1} h^{-1}) were determined from Eq. 8.

$$P_i = \frac{S_i X F_{A0}}{n_i W} \tag{8}$$

Here S_i, n_i and X have the same meaning as before, F_{A0} is the carbon monoxide molar feed rate and W is the catalyst mass.

Mass specific initial carbon monoxide reaction rates (i.e. reaction rates extrapolated to null conversion), r_{A0} (mol kg^{-1} h^{-1}), were calculated from CO conversions,

assuming that carbon monoxide conversion follows an apparent first order rate law with respect to its concentration [28], which, when applied to a CSTR, gives Eq. 9.

$$r_{A0} = \frac{XF_{A0}}{W(1-X)} \tag{9}$$

Here the symbols X, F_{A0} and W have the same meaning as before.

Finally, area-specific reaction rate relative to copper surface area, r'_{A0} (mmol m^{-2} h^{-1}) was calculated dividing the reaction rate from Eq. 9 by the experimentally copper metal surface area, S_{Cu} (m^2 g^{-1}), as shown in Eq. 10.

$$r'_{A0} = \frac{r_{A0}}{S_{Cu}} \tag{10}$$

Results and discussion

Characterization of the oxides

The mixed-oxides were prepared by calcination of co-precipitated hydroxy-carbonates, whose X-ray diffractograms are shown in Fig. S1. They consist largely of a hydrotalcite-type hydroxycarbonate (LDH) phase with minor amounts of a rhodochrosite ($MnCO_3$) phase.

Chemical composition and surface area

Table 1 shows the chemical composition of the oxides prepared by calcination of the precursor LDH at 673 K determined by ICP-OES. Comparing the values in the second column of Table 1 with the numbers that appear in the nomenclature of the

Table 1 Chemical composition and specific surface area of the oxides

Material	Metal molar fractions[a]		Cu load (wt%)[a]	Mn or Zn incorporation (%)[b,d]	S_{BET} (m^2 g^{-1})
	Cu/Mn or Cu/Zn[b]	Al/M[c]			
CuMn2AlC	2.8	0.21	49.6	79	62
CuMn1AlC	1.5	0.22	40.0	78	101
CuMn0.5AlC	1.1	0.25	31.4	65	104
CuMn0.2AlC	0.29	0.24	13.5	87	145
CMSC	(2.0)[b]	0.16	46.5	–	84
CuZn2AlC	(2.0)[b]	0.16	46.3	(99)	55

[a]Determined by ICP-OES

[b]Values between parentheses correspond to Zn rather than Mn

[c]M is the total of metal elements (Al + Cu+ Zn or Mn)

[d]Percent Mn or Zn in the oxides, relative to the nominal ones

catalysts, which give the nominal molar Cu/Mn or Cu/Zn ratios, it is seen that not all the manganese used in the syntheses was incorporated into the solids. The fifth column in the Table gives the percentage of the manganese that was incorporated relative to the nominal ones. This may be related to the larger size of the Mn^{2+} ion in octahedral coordination (0.80 Å) as compared to Mg^{2+} (0.65 Å) which may limit the incorporation of Mn^{2+} into the LDH structure. The analytical Cu/Zn ratio of a Cu–Zn–Al material (CuZn2AlC) was the same as the nominal one.

Because of the low manganese incorporation into the hydroxycarbonate precursors, the actual content from both, copper, and aluminum, were higher than expected from the nominal composition. The analytical molar ratio of aluminum to total metal ions was somewhat higher than the targeted 0.19 value in the case of the Cu–Mn–Al materials. In the case of the synthetized Cu–Zn–Al material, the targeted aluminum to total metal elements was the same as that in CMSC, therefore the actual catalyst composition was the same as the nominal one (0.16).

The specific surface areas of the calcined materials are also displayed in Table 1 and show that mixed oxides based on Cu–Mn–Al with a considerably higher surface area than the synthetized Cu–Zn–Al methanol synthesis catalysts were obtained. The specific surface area is seen to increase monotonically with the manganese content of the solids. Therefore, manganese can be considered as a textural promoter of the Cu–Al system.

X-ray diffraction

The XRD patterns of the materials are presented in Fig. 1. They were collected using a synchrotron light source, at LNLS (Brazil). Due to limited beam time availability,

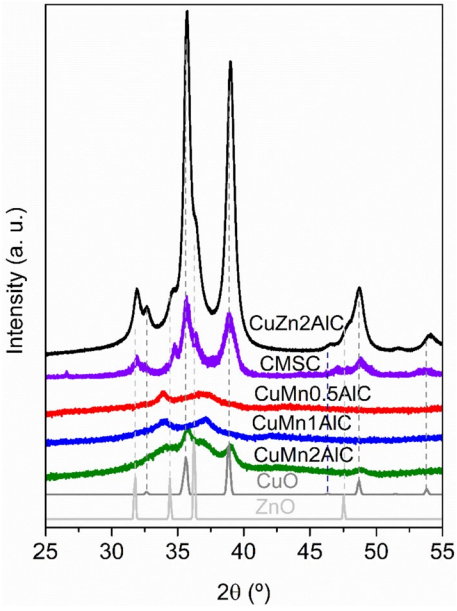

Fig. 1 XRD of the mixed-oxides and CuO (ICSD 16025) and ZnO (ICSD180052) patterns

the sample CuMn0.2AlC was not measured in this laboratory. However, it was run in conventional XRD, and the pattern is shown in Fig. S2. From Fig. 1 it is possible to see that the more crystalline materials were those containing Cu, Zn and Al metals. Both the commercial (CMSC) and the synthetized (CuZn2AlC) Cu–Zn–Al oxides display the characteristic peaks of CuO (ICSD 16025) and ZnO (ICSD 180052) phases. The diffraction patterns for the Cu–Mn–Al oxides are broader than for the Zn containing ones, with some overlapping peaks of low intensity. Only the CuMn2AlC oxide, with the highest copper content, displayed peaks at 2θ ca. 36° and 39° attributable to CuO.

The CuMn0.2AlC oxide (cf. Fig. S2), the one with the highest manganese content, exhibited somewhat more defined peaks, which allowed the proposal of a phase assignment, namely a mixture of MnO_2 and a spinel-like Mn–Al phase. Fig. S2 presents the XRD patterns of the phases. All other Cu–Mn–Al oxides display small peaks at 2θ ca. 34° and 37° (Fig. 1). The latter coincides with the main MnO_2 X-ray diffractions, but the former could not be assigned to any manganese or copper-manganese phase. As its intensity increases with increasing manganese content, it is most probably related to a manganese-containing phase.

In situ reduction studies

XANES results

Fig. 2a and b show the Mn K-edge XANES and first derivative spectra for the materials reduced in situ at 529 K (same reduction temperature used in the catalytic tests) at atmospheric pressure under a 5 V% hydrogen in helium mixture and those of reference materials. The assignment of the species present in the samples is more conveniently made with reference to the first derivative spectra. The absorption edge energy, as measured from the position of the first intense maximum in the first derivative spectrum is the same as that of MnO at 6545 eV for all materials. Besides, the main features of the MnO spectrum appear in the spectra of the reduced materials, as shown by the dashed lines in Fig. 2a and b. There is however a distinct maximum at ca. 6547 eV, marked by the solid line in Fig. 2b, that does not exist in the first derivative spectrum of MnO and coincides with the absorption edge energy of Mn_3O_4. Furthermore, the $1s \rightarrow 3d$ pre-edge transition is stronger in the Cu–Mn–Al reduced materials than in MnO and similar to that of Mn_3O_4. Therefore, these materials contain both a MnO like phase and a Mn_3O_4 phase.

The XANES spectra at the Cu K-edge and first derivatives for the reduced materials are presented in Fig. S3. All spectra are practically the same as that of copper metal. In all cases the absorption edge energy was that same as that of a copper foil at 8979 eV, except for the catalysts with the smallest copper content, where an 0.6 eV red shift was observed.

EXAFS results

The EXAFS oscillations and the magnitude and imaginary parts of the Fourier transform (FT) for the in situ reduced oxides are shown in Figs. S4 to Fig. S12, both

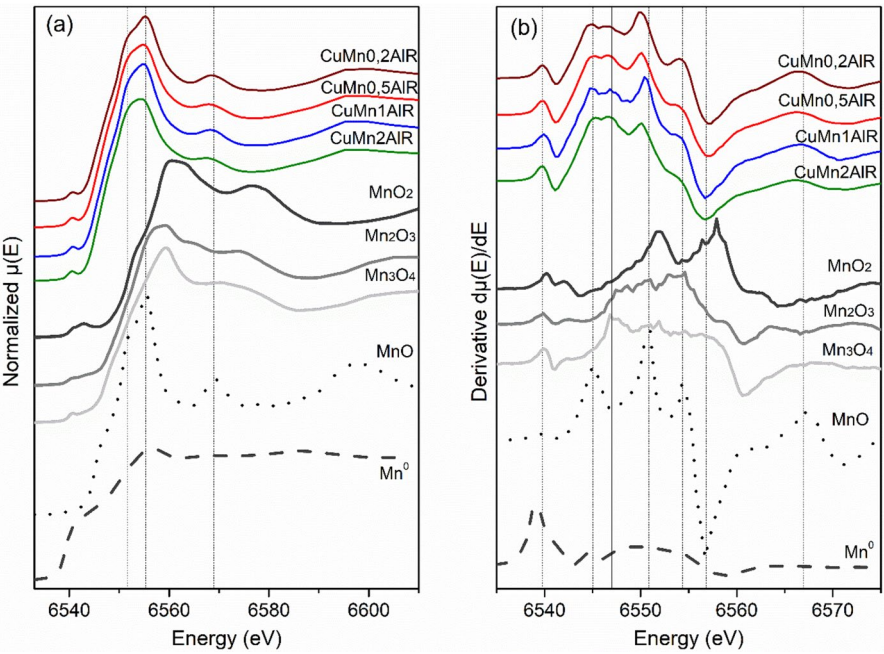

Fig. 2 XANES spectra (**a**) and derivative spectra (**b**) for the materials reduced in situ at 538 K and standards at the Mn K-edge

at the Mn and Cu K-edges. The structural parameters obtained from the EXAFS spectra at the Mn K-edge are displayed in Table 2. In order to reduce the simulations uncertainties and parameter correlations, only one Mn–O and one Mn–Mn distance were considered. Also, the first sphere coordination number of manganese was fixed at 6 which is the total number of oxygen atoms in the first shell (multiple paths were not considered). It is important to emphasize here that the usage of a more detailed model to describe the manganese oxides did not produce reliable results, leading

Table 2 Structural parameters obtained from EXAFS results at the Mn K-edge for the reduced materials

Sample	R_{Mn-O} (Å)[a]	N_{Mn-O}[b]	σ^2_{Mn-O} (Å^2)[c]	R_{Mn-Mn} (Å)[a]	N_{Mn-Mn}[d]	σ^2_{Mn-Mn} (Å^2)[e]	R_{factor}
CuMn0.2AlR	2.06(2)	6.0	0.024(4)	3.05(4)	2.0(2)	0.013(3)	0.041
CuMn0.5AlR	2.09(2)	6.0	0.024(4)	3.08(4)	2.2(2)	0.015(3)	0.032
CuMn1AlR	2.07(2)	6.0	0.024(4)	3.08(4)	2.1(2)	0.014(3)	0.020
CuMn2AlR	2.09(2)	6.0	0.024(4)	3.08(4)	2.2(2)	0.013(3)	0.048

[a]Average interatomic distances

[b]Average coordination number in the first shell fixed in 6.0

[c]Debye–Waller factor for Mn–O path

[d]Average coordination number in the second shell

[e]Debye–Waller factor for Mn–Mn path. Uncertainties for all parameters are shown between parentheses

to impossible parameter values and non-convergence of the Levenberg–Marquadt minimization algorithm.

According to the XANES results, these samples contain manganese(II) oxide, probably in admixture with a Mn_3O_4 phase. Manganese(II) oxide has a simple cubic structure, with both manganese and oxygen octahedrally coordinated by each other [35]. The Mn–O and Mn–Mn distances in the crystalline materials are 2.22 and 3.14 Å [35]. The Mn_3O_4 structure is considerably more complex; it is a regular spinel structure, with Mn^{2+} ions at tetrahedral sites and Mn^{3+} ions at octahedral sites, with considerable Jahn–Teller distortion [35, 36]. The Mn^{2+}–O distance is 2.04 Å, while the Mn^{3+} ion has four oxide neighbors at 1.93 Å and two others at 2.28 Å [35, 36]. As a result, the average oxide first shell distance is 2.03 Å. There are two second shell Mn–Mn distances, averaging 3.04 Å [35]. Therefore, our best fit distance parameters with a simplified model lie between those of crystalline MnO and Mn_3O_4, confirming the XANES results that pointed to the existence of mixed manganese valence states in the reduced materials. Furthermore, the small second sphere coordination numbers indicate structural disorder beyond the first coordination sphere. This structural disorder, plus the fact that each of the peaks in the FT spectra may contain the contribution of species with multiple environments may account for the large Debye–Waller factors found.

The structural parameters obtained from the EXAFS spectra at the Cu K-edge are displayed in Table 3. In the case of the Cu K-edge for the reduced materials, where the XANES, and also the XRD results shown in the next section, indicate that metallic copper is the only copper species observed, the adjustable parameters were the average coordination numbers, distances and Debye-Waller factors of the first three coordination spheres.

The results in Table 3 indicate progressive decrease in Cu–Cu bond distances with decreasing copper content. Table also includes the results for the Cu–Zn–Al catalyst, that has similar bond distances as the Cu–Mn–Al catalyst with the largest copper content. At the same time, the coordination numbers for all coordination shells decrease with decreasing copper content, the largest relative difference being for the catalyst with the smallest copper content. Both trends are certainly related with a copper crystallite size that decreases with decreasing copper content. The smaller the crystallites, the larger the fraction of atoms with incomplete coordination shells due to increasing surface to volume ratio. The same factor causes the average bond contraction due to increasing excess surface free energy with increasing surface to volume ratio.

X-ray diffraction

The XRD patterns for the materials after reduction under 5% H_2 in He up to 529 K are shown in Fig. 3. The main peak in all the samples corresponds to metallic copper. However, small broad peaks also appear in the Mn containing samples, related to a MnO phase, in agreement with the XANES data. Crystalline ZnO still remains in CuZn2AlC after reduction. These results indicate that the copper in the calcined samples is totally reduced to metallic Cu under the present reduction conditions.

Table 3 Structural parameters obtained from EXAFS results at the Cu K-edge for the reduced materials

Sample	N_1[a]	R_1[b] (Å)	σ_1^2(Å^2)[c]	N_2[a]	R_2[b] (Å)	σ_2^2(Å^2)[c]	N_3[b]	R_3[b] (Å)	σ_3^2(Å^2)[c]	R_{factor}
CuMn0.2AlR	7.3(4)	2.513(3)	0.01(1)	4.7(3)	3.554(4)	0.016(2)	6.5(5)	4.352(4)	0.015(3)	0.027
CuMn0.5AlR	9.7(4)	2.520(3)	0.01(1)	6.0(3)	3.564(4)	0.016(2)	10.5(5)	4.365(4)	0.017(3)	0.018
CuMn1AlR	10.3(4)	2.528(3)	0.01(1)	6.4(3)	3.575(4)	0.016(2)	12.4(5)	4.379(4)	0.015(3)	0.024
CuMn2AlR	10.6(4)	2.536(3)	0.01(1)	7.0(3)	3.586(4)	0.016(2)	13.8(5)	4.392(4)	0.015(3)	0.032
CuZn2AlR	10.7(4)	2.536(3)	0.01(1)	6.8(3)	3.586(4)	0.016(2)	16.3(5)	4.392(4)	0.015(3)	0.027

[a]N_i is the average coordination number for the coordination shell i

[b]Rj is the average distance for the coordination shell j

[c]σ_i is the Debye–Waller factor for the coordination shell i. Uncertainties in all parameters are shown between parentheses

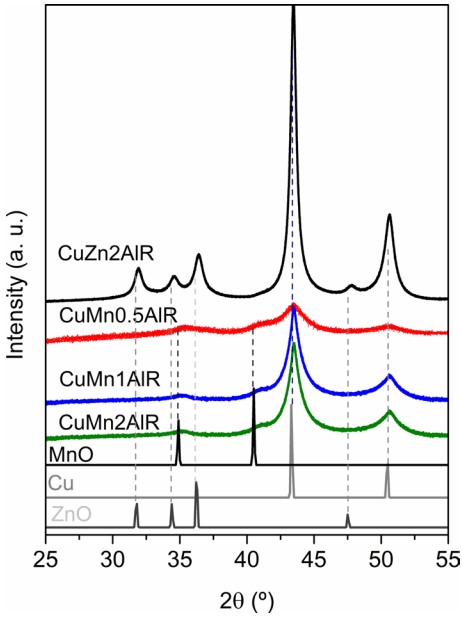

Fig. 3 XRD of the materials after in situ reduction under 5% H_2 in He up to 538 K and MnO (ICSD 162039), Cu (ICSD 627113) and ZnO (ICSD180052) patterns

In Figs. S13–S16, the evolution of the XRD during the reduction process is shown. Some selected diffractograms were plotted from room temperature to 529 K (ramp of 10 K min^{-1} and isothermal at 538 K for 20 min).

It can be confirmed that the Mn containing samples begin with a very disordered structure. In the case of the sample with Zn instead of Mn (Fig. S16), the starting structure, already organized before reduction, becomes even more defined, with sharper peaks, with increasing temperature. In all samples, reduction starts before the temperature plateau is reached. The onset of reduction is at 487 K with CuZn2AlC (Fig. S16), 493 K with CuMn2AlC (Fig. S14) and 513 K with CuMn1AlC (Fig. S14), and CuMn0.5AlC (Fig. S13). Therefore, the reducibility of the copper is smaller with the Cu–Mn–Al materials than the Cu–Zn–Al one and decreases with increasing manganese content.

Copper crystallite sizes in the reduced materials were determined using the Scherrer equation and are displayed in the last column of Table 4. Copper crystallite sizes increase with increasing Cu/Mn ratio, and this may be a combined result of decreasing specific surface area of the oxides and increasing tendency for sintering of copper in the same direction. All manganese-containing catalysts had smaller copper particle sizes than the zinc containing one prepared by the same method.

Hydrogen reduction and N_2O decomposition measurements

The total hydrogen consumption during the temperature programming followed by an isothermal step is of interest and is presented in Table 4, together with the oxygen titration results. In this table, hydrogen consumption is presented as the ratio of moles of hydrogen consumed in the experiments to the ones expected for complete

Table 4 Crystallites and reduction properties of metallic copper

Material	d_c(XRD) (nm)[a]	H_2-TPR (n_{H2}/n_{Cu})[b]	Dispersion (%)[c]	S_{Cu} ($m^2\ g^{-1}$)[d]	d_c (nm)[e]
CuMn2AlR	8.8	1.2	11	36	9.2
CuMn1AlR	8.4	1.3	17	46	5.9
CuMn0.5AlR	4.1	1.5	22	47	4.5
CuMn0.2AlR	n.a.[f]	2.4	76	69	1.3
CuZn2AlR	16.5	1.1	11	33	10
CMSCR	n.a.[f]	1.1	8	24	13

[a]Crystallite size determined from the Scherrer equation

[b]Moles H_2 consumed per mole Cu

[c]Determined by the N_2O decomposition method

[d]Copper metal surface area

[e]Crystallite size determined by the N_2O decomposition method

[f]Not available

reduction of the CuO present in each catalyst to the metallic state, which coincides with their copper mole content. For CMSC and CuZn2AlC, that contain zinc instead of manganese, this ratio was 1.1, suggesting a small reduction of the zinc. It has been proposed that the hydrogen dissociated on the copper surface may reduce ZnO at the Cu^0–ZnO interface [37]. With Cu–Mn–Al materials, the ratio increases continuously with manganese content, up to 2.4, indicating substantial reduction of the manganese. Quantification of the degree of reduction of manganese is not possible, due to uncertainty in the proportion of manganese oxidation states both in the oxide and in the reduced state of the materials.

Both the in situ XRD and XANES results showed that copper was completely reduced to the metallic state upon exposure of the materials to hydrogen at 538 K. Therefore, in the calculation of the copper dispersion in the N_2O decomposition experiments, it was assumed that copper was completely reduced after the initial TPR. The results for the dispersion and derived copper surface area and crystallite size, are also presented in Table 4.

The dispersion of CuMn2AlR is close to that of CuZn2AlR but dispersion increases pronouncedly with manganese content. The average crystallite diameters calculated from the dispersions vary correspondingly in the opposite direction. It is noteworthy that the average crystallite diameters determined by the N_2O decomposition method are close to and vary in the same direction as the ones calculated using the Scherrer equation. These results are also consistent with the ones obtained from EXAFS at the Cu K-edge, that showed decreasing first, second and third sphere coordination number with decreasing copper content (cf. Table 3).

The metal surface area depends on dispersion and metal content and, since the dispersion increases with decreasing copper content, the metal surface areas, although varying considerably, do not vary as much as the dispersions in relative terms. Two main factors may contribute to the increase in dispersion with decreasing copper content: first, the specific surface areas of the precursor oxides increase

in the same direction (cf. Table 1), which may facilitate the dispersion of the copper in the reduced catalysts; second, the increase in copper concentration in the catalysts may favor crystallite growth by sintering. In this connection, Fig. S17 shows a plot of average copper crystallite diameter vs. copper wt% and a linear correlation is obtained. It is worthy of note that the copper in the Cu–Zn–Al catalyst prepared by our method, using sodium-free starting materials has a better dispersion than in the industrial catalyst with the same elements and composition.

Catalytic measurements

Methanol synthesis

The catalysts were tested in the methanol synthesis reaction dispersed in a *n*-hexadecane suspension in a CSTR reactor, at 538 K and 50 bar hydrogen pressure. Carbon monoxide conversion vs. time-on-stream is shown in Fig. 4. The data show that, after an initial fast deactivation, the catalysts were stable for the ca. 8 h duration of the experiments. As the catalyst masses used were chosen so that the quantity of copper in each experiment was approximately the same, the conversions obtained approximately reflect catalytic activity per amount of copper. On this basis, except for CuMn2AlR, all Cu–Mn–Al catalysts were more active than the Cu–Zn–Al ones.

Table 5 shows that, except for CuMn0.2AlR, all catalysts prepared in this work had similar productivities in terms of methanol produced per total catalyst mass, which were significantly higher than that of the industrial Cu–Zn–Al catalyst, CMSCR. From the carbon monoxide conversion results, mass- and area-specific (with respect to copper surface area) reaction rates for each experiment were calculated (see third and fourth column of Table 5). Again, except for CuMn0.2AlR, the reaction rates were essentially the same among the Cu–Mn–Al materials. The area-specific reaction rate values for the Cu–Zn–Al catalysts were similar to each other, but somewhat higher than those of the Cu–Mn–Al catalysts.

As shown in our previous paper [17], the area-specific reaction rate on a Cu–Al catalyst also obtained from a LDH precursor was close to those of the Cu–Mn–Al catalysts, but its selectivity to methanol was considerably smaller (48.7% vs 94.5%), mainly due to dehydration of methanol to DME and to the methanation reaction. Thus, the main promoting effects of manganese or zinc are to improve the selectivity to methanol.

The results obtained with the Cu–Zn–Al catalyst prepared by the method described here show that zinc has a larger influence on the copper-based reaction rate than manganese. This could arise from some direct participation of the promoters in the reaction mechanism or from some influence on the intrinsic properties of copper, which could not be detected in our XANES measurements.

It is relevant that it has recently been found that methanol synthesis on copper is a structure sensitive reaction and the copper-based area-specific reaction rate was found to decrease with decreasing copper particle size. The Cu particle sizes on the Cu–Zn–Al catalysts used in the present paper are larger than the ones on the Cu–Mn–Al catalyst (cf. Table 4). This structure-sensitivity effect may also explain

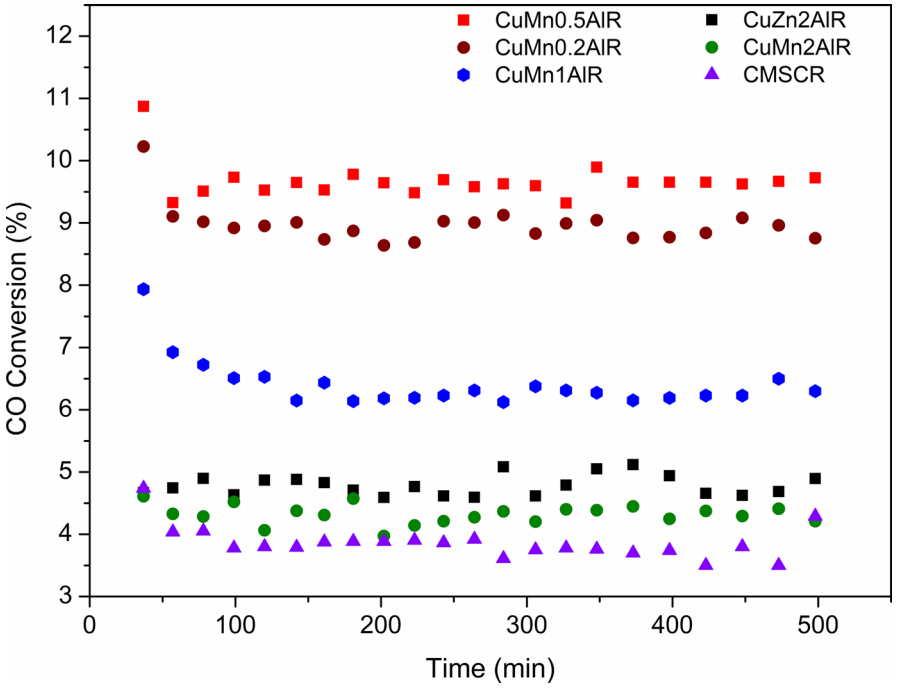

Fig. 4 Carbon monoxide conversion vs. time-on-stream in CO hydrogenation at 538 K and 50 bar in a CSTR reactor with the catalysts suspended in *n*-hexadecane

Table 5 Methanol synthesis results (liquid phase, 583 K, 50 bar)

Material	Productivity[a]	Reaction rate[b] (mol kg^{-1} h^{-1})	Reaction rate[c] (mmol m^{-2} h^{-1})	Selectivity (%)[d]			
				CH_3OH	$(CH_3)_2O$	CH_4	CO_2
CuMn2AlR	31 (± 3)	34.9	0.97	92.0	1.0	2.2	4.8
CuMn1AlR	35 (± 6)	39.4	0.86	94.1	0.7	1.5	3.7
CuMn0.5AlR	36 (± 1)	42.6	0.91	93.6	0.8	0.3	5.3
CuMn0.2AlR	16 (± 2)	19.7	0.29	92.3	1.8	1.1	4.7
CuZn2AlR	33 (± 3)	38.5	1.17	91.6	1.9	1.6	4.8
CMSCR	25 (± 2)	28	1.17	88.3	3.5	1.7	6.6

[a]Moles of methanol produced per kg catalyst per hour

[b]Relative to catalyst mass

[c]Relative to copper surface area

[d]Percentage of moles CO converted to each product per mole converted

the very low reaction rate obtained with CuMn0.2AlR, where the average particle size estimated from N_2O decomposition was only 1 nm. It is relevant that this was the only catalyst in which a change in the electronic charge of Cu atoms could be observed by XANES with respect to the remaining materials.

The selectivity to methanol of all catalysts prepared here, including the Cu–Zn–Al catalyst, was larger than that of the industrial catalyst, mainly on account of smaller selectivities to DME and carbon dioxide. CuMn0.5AlR and CuMn1AlR, besides presenting the largest methanol productivities among all catalysts, also had the largest methanol selectivities.

If we ignore the atypical CuMn0.2AlR catalyst with its very small copper particle size, it is seen that increasing manganese content decreases the methanation selectivity. It is already known from the literature that a higher proportion of Mn^{2+} and Mn^{3+} on the surface can significantly affect the catalytic properties of MnOx containing materials [38, 39]. These low charged manganese atoms can generate relatively stable oxygen vacancies which will promote lattice oxygen mobility and the dissociation of CO_2 producing surface oxygen intermediates that can react with carbon deposits (CH_x species—methane precursors [40, 41]), thus hindering the methanation reaction. This process is more evident in the catalysts with higher manganese content.

Under the present testing conditions, the best Cu–Mn–Al catalysts prepared presented some advantage in terms of methanol productivity and selectivity over the Cu–Zn–Al ones. The productivity of the Cu–Mn–Al catalysts seems to be dictated by an interplay of copper dispersion and copper content. Decreasing Cu/Mn ratio decreases the copper content but increases the dispersion (cf. Table 4). Overall, the copper surface area increased with decreasing Cu/Mn ratio, but below a certain crystallite diameter the intrinsic activity of copper decreases, so maximum productivity is obtained over a limited range of Cu/Mn ratios.

In order to compare the results with one using bimetallic Cu–Al catalyst, our previous paper [17] shows that this catalyst exhibited the lowest Cu dispersion (5.3%) and highest copper particle size (18.8 nm), when compared with the Cu–Mn–Al catalysts. The selectivity to methanol was only 48.7%. This demonstrates the positive effect of Mn in the trimetallic Cu–Mn–Al catalysts.

DME synthesis

The two best Cu–Mn–Al catalysts in terms of methanol productivity, CuMn1AlR and CuMn0.5AlR, plus the synthetized and the industrial Cu–Zn–Al catalysts were tested as the methanol synthesis component in a mixed catalyst system with a γ-alumina as the methanol dehydration component, in the direct syngas to DME conversion. The catalyst masses were selected to have the same copper content in the reactor in each experiment. The alumina amount was chosen to have the same 0.41 Cu/Al ratio in the reactor in all experiments, considering the aluminum content in each methanol synthesis catalysts.

The reaction products observed were the same as in methanol synthesis, except methane, that was produced in negligible amount in the DME synthesis experiments. Fig. 5 shows the carbon monoxide conversion vs. time on stream curves.

As in the case of methanol synthesis, except for an initial deactivation, the catalysts were stable for the duration of the experiments. The order of carbon monoxide conversions was the same as in methanol synthesis, which suggests that methanol synthesis rather methanol dehydration is the rate-determining process in the overall

reaction. The carbon monoxide conversion on CuMn0.5AlR relative to that on the other catalysts was larger in DME than in methanol synthesis.

Table 6 displays DME productivity (per methanol synthesis catalyst mass), reaction rates and selectivity of the tested catalysts in the DME synthesis experiments. As expected, the reaction rate values are considerably larger in DME than in methanol synthesis, because the water produced in methanol dehydration on alumina drives the WGSR on the methanol synthesis catalyst, producing carbon dioxide, that is generally considered to be the actual methanol precursor in the synthesis reaction [18, 19]. The increase in carbon dioxide concentration in the reaction medium increases the rate of the catalytic cycle.

The selectivity results do not show significant differences among the catalysts. The Cu–Mn–Al catalysts have a slightly smaller selectivity to methanol than the Cu–Zn–Al ones. The DME/CO_2 selectivity ratio is about 2, showing that in all cases the overall reaction is represented by Eq. (5) shown in the Introduction, i.e., essentially all the water produced in methanol dehydration is consumed in the WGSR to generate carbon dioxide.

The productivity and reaction rates result for CuMn1AlR and the Cu–Zn–Al catalysts follow the same tendency as in methanol synthesis, i.e., a larger DME productivity and a smaller area-specific reaction rate with the Cu–Mn–Al catalyst. CuMn0.5AlR, however has a considerably larger DME productivity than the other catalysts and a larger area-specific reaction rate than CuMn1AlR. One possible

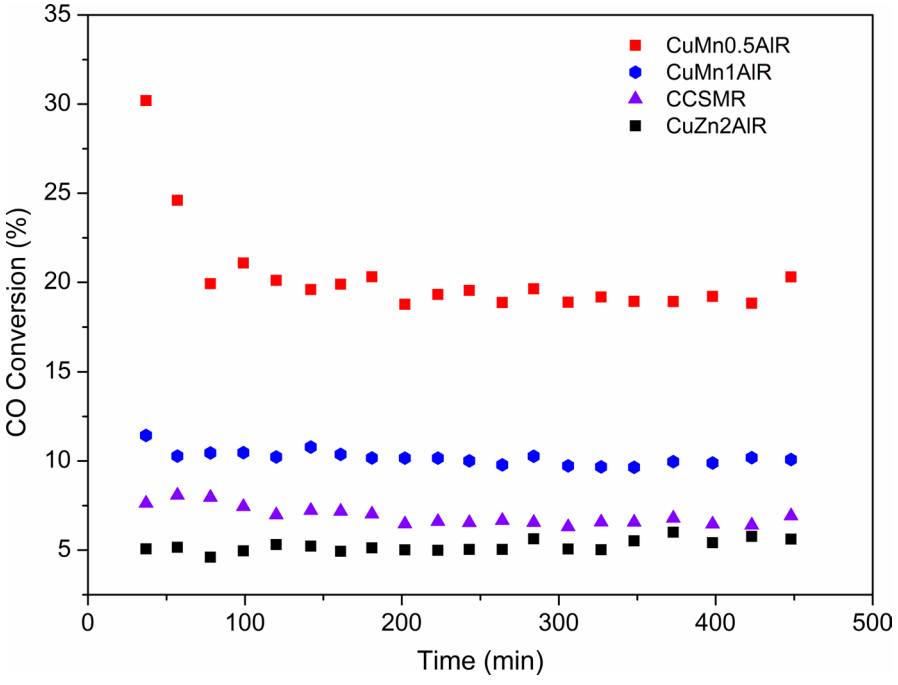

Fig. 5 Carbon monoxide conversion vs. time-on-stream in CO + H_2 direct conversion to DME at 538 K and 50 bar in a CSTR reactor with the catalysts plus γ-alumina suspended in *n*-hexadecane

Table 6 Direct syngas to DME conversion (liquid phase, 583 K, 50 bar)

Material	Productivity[a]	Reaction rate[b] (mol kg^{-1} h^{-1})	Reaction rate[c] (mol m^{-2} h^{-1})	Selectivity (%)[d]			
				CH_3OH	$(CH_3)_2O$	CH_4	CO_2
CuMn1AlR	38 (± 3)	68	1.5	5.0	62.0	0.0	33.0
CuMn0.5AlR	61 (± 5)	119.9	2.6	6.0	63.0	0.0	31.0
CuZn2AlR	32 (± 10)	56.9	1.7	7.0	61.0	0.0	31.0
CMSCR	30 (± 9)	51.8	2.2	7.0	62.0	0.0	31.0

[a]Moles of DME produced per kg methanol synthesis catalyst per hour

[b]Relative to catalyst mass

[c]Relative to copper surface area

[d]Percentage of moles CO converted to each product per mole converted

explanation comes from Table 5. This catalyst has a higher CO_2 selectivity in methanol synthesis than CuMn1AlR and thus presumably a better WGSR activity, which may accelerate the DME catalytic cycle. This advantage of CuMn0.5AlR over CuMn1AlR is not observed in methanol synthesis, i.e., in the absence of alumina, because these catalysts have low methanol dehydration and methanation activities that could provide water to drive the WGSR.

In terms of the characterization methods used some differences may be observed between CuMn0.5AlR and CuMn1AlR. The most conspicuous one is observed in Fig. 3, where the copper in the former catalyst is seen to be less crystalline than the latter. This is reflected in the smaller copper crystallite diameter derived from the Scherrer equation, shown in Table 4, and in the smaller Cu–Cu distance in CuMn0.5AlR derived from EXAFS, as shown in Table 3. According to the literature [38], this better WGSR activity can be due to the surface oxygen vacancies (see the previous section) formed on manganese oxide surfaces with higher proportion of Mn^{2+} and Mn^{3+}. These vacancies can act as anchoring sites for water molecules that will react with CO adsorbed on copper generating a formate intermediate essential to the WGSR reaction. The results in Table 4 show a larger hydrogen consumption during TPR with CuMn0.5AlR than with CuMn1AlR, suggesting a larger amount of reduced Mn species in the former.

Conclusions

All the Cu–Mn–Al oxides prepared here had low crystallinity, in contrast with Cu–Zn–Al mixed oxides (obtained either from a commercial supplier or synthetized in our laboratory by the same method as the manganese-containing oxides).

After reduction at 538 K, the copper was completely reduced to the metallic state and the manganese was reduced mainly to MnO, but with the presence of some Mn^{3+}, probably as a Mn_3O_4 phase.

The copper dispersion decreased markedly with increasing copper content but the dispersion in a Cu–Mn–Al catalyst was close to that of a Cu–Zn–Al catalyst

with similar copper content prepared in our lab. In both materials the copper dispersion was larger than in an industrial Cu–Zn–Al catalyst (CMSC).

The productivity for methanol production based on total catalyst mass for the Cu–Mn–Al catalysts with Cu/Mn ratio in the 1.1–2.8 range was close to that of the Cu–Zn–Al catalyst with Cu/Zn equals 2.0, and higher than that of CMSC also with a 2.0 Cu/Zn ratio. The copper-based area-specific reaction rate was similar among the Cu–Mn–Al catalysts with Cu/Mn ratio in the 1.1–2.8 range and smaller than that of both Cu–Zn–Al catalyst, which were close to each other. The methanol selectivity was higher with the best Cu–Mn–Al catalysts (CuMn0.5Al and CuMn1Al), as compared to the Cu–Zn–Al ones.

When comparing the two best Cu–Mn–Al catalysts with the Cu–Zn–Al ones in the direct syngas to DME reaction, using a γ-alumina as the methanol dehydration component, the same order of productivity based on the hydrogenation catalyst is found as in methanol synthesis, but the productivity of CuMn0.5Al (with real Cu/Mn ratio equals 1.1) stood out from the others, possibly on account of a larger WGSR activity that plays an important role in the DME synthesis reaction network.

Overall, replacing Zn with Mn and increasing the Mn proportion has advantages, in that this allows the obtention of precursor mixed oxides with higher specific surface areas, allows the production of smaller copper crystallites upon reduction and has beneficial chemical effects in terms of selectivity in methanol synthesis and productivity in syngas to DME conversion.

The purpose of this paper was to compare de CuMnAl catalysts with a CuZnAl one prepared by the same method. There are many conceivable preparation methods for these ternary catalysts, but the use of LDH precursors is convenient from a practical standpoint, due to the experimental easiness and reproducibility of their preparation. The comparison with the commercial catalyst showed that the CuZnAl catalyst obtained by the method used here was at least as good as the commercial one, both in methanol and in DME synthesis.

Supplementary Information The online version contains supplementary material available at https://doi.org/10.1007/s11144-024-02581-6.

Acknowledgements The authors acknowledge the XRD at IQ-UFRJ for sample analysis. To the Laboratório de Petróleo e Meio Ambiente (LCPMA) at UERJ for making available the equipment to perform the TPR and N_2O decomposition measurements. We acknowledge LNLS (Campinas, Brazil) for provision of synchrotron radiation facilities for XAS measurements at XAFS2 beamline (Project 20190122) and XRD measurements at XPD (Project 20190118) beamline. The authors also thank Conselho Nacional de Desenvolvimento Científico e Tecnológico—CNPq (Grant 426600/2018-5) Brazil, for the financial support. ACFJ thanks CNPq for a productivity research scholarship. This study was financed in part by the Coordenação de Aperfeiçoamento de Pessoal de Nível Superior-Brasil (CAPES)—Finance Code 001. HB thanks CAPES for a D.Sc. scholarship.

Author contributions The manuscript was written through contributions of all authors. All authors have given approval to the final version of the manuscript.

Funding Funding was provided by Conselho Nacional de Desenvolvimento Científico e Tecnológico (Grant No. 426600/2018-5), Coordenação de Aperfeiçoamento de Pessoal de Nível Superior (Grant No. 001).

Declarations

Competing interests The authors have no competing interests to declare that are relevant to the content of this article.

References

1. Bepari S, Kuila D (2020) Steam reforming of methanol, ethanol and glycerol over nickel-based catalysts-a review. Int J Hydrogen Energy 45:18090–18113. https://doi.org/10.1016/j.ijhydene.2019.08.003
2. Dos Santos RG, Alencar AC (2020) Biomass-derived syngas production via gasification process and its catalytic conversion into fuels by Fischer–Tropsch synthesis: a review. Int J Hydrogen Energy 45:18114–18132. https://doi.org/10.1016/j.ijhydene.2019.07.133
3. Sousa-Aguiar EF, Noronha FB, Faro A Jr (2011) The main catalytic challenges in GTL (gas-to-liquids) processes. Catal Sci Technol 1:698–713. https://doi.org/10.1039/C1CY00116G
4. Jadhav SG, Vaidya PD, Bhanage BM, Joshi JB (2014) Catalytic carbon dioxide hydrogenation to methanol: a review of recent studies. Chem Eng Res Des 92:2557–2567. https://doi.org/10.1016/j.cherd.2014.03.005
5. Ali KA, Abdullah AZ, Mohamed AR (2015) Catalytic carbon dioxide hydrogenation to methanol: a review of recent studies. Renew Sustain Energy Rev 44:508–518. https://doi.org/10.1016/j.rser.2015.01.010
6. Çelik MB, Özdalyan B, Alkan F (2011) The use of pure methanol as fuel at high compression ratio in a single cylinder gasoline engine. Fuel 90:1591–1598. https://doi.org/10.1016/j.fuel.2010.10.035
7. Joghee P, Malik JN, Pylypenko S, O'Hayre R (2015) A review on direct methanol fuel cells—in the perspective of energy and sustainability. MRS Energy Sustain 2:1–31. https://doi.org/10.1557/mre.2015.4
8. Galadima A, Muraza O (2015) From synthesis gas production to methanol synthesis and potential upgrade to gasoline range hydrocarbons: a review. J Nat Gas Sci Eng 25:303–316. https://doi.org/10.1016/j.jngse.2015.05.012
9. Bakhtyari A, Rahimpour MR (2018) Methanol. In: Basile A, Dalena FBT-M (eds) Methanol to dimethyl ether. Elsevier, Amsterdam, pp 281–31
10. Prabowo B, Yan M, Syamsiro M, Setyobudi RH, Biddinika MK (2017) State of the art of global dimethyl ether production and its potentional application in Indonesia. Proc Pak Acad Sci Part B 54:29–39
11. Arcoumanis C, Bae C, Crookes R, Kinoshita E (2008) The potential of di-methyl ether (DME) as an alternative fuel for compression-ignition engines: a review. Fuel. 87:1014–1030. https://doi.org/10.1016/j.fuel.2007.06.007
12. Zhu Y, Wang S, Ge X, Liu Q, Luo Z, Cen K (2010) Experimental study of improved two step synthesis for DME production. Fuel Process Technol 91:424–429. https://doi.org/10.1016/j.fuproc.2009.05.001
13. Nakyai T, Saebea D (2019) Exergoeconomic comparison of syngas production from biomass, coal, and natural gas for dimethyl ether synthesis in single-step and two-step processes. J Clean Prod 241:118334. https://doi.org/10.1016/j.jclepro.2019.118334
14. Takeishi K (2010) Dimethyl ether and catalyst development for production from syngas. Biofuels 1:217–226. https://doi.org/10.4155/bfs.09.16
15. Saravanan K, Ham H, Tsubaki N, Bae JW (2017) Recent progress for direct synthesis of dimethyl ether from syngas on the heterogeneous bifunctional hybrid catalysts. Appl Catal B 217:494–522. https://doi.org/10.1016/j.apcatb.2017.05.085
16. Ogawa T, Inoue N, Shikada T, Ohno Y (2003) Direct dimethyl ether synthesis. J Nat Gas Chem 12:219–227
17. Blanco H, Lima SH, Rodrigues V, Palacio LA, Faro A Jr (2019) Copper–manganese catalysts with high activity for methanol synthesis. Appl Catal A 579:65–74. https://doi.org/10.1016/j.apcata.2019.04.021

18. Kagan YB, Rozovskij AY, Liberov LG, Slivinskij EV, Lin GI, Loktev SM, Bashkirov AN (1975) Study of mechanism of methanol synthesis from carbon monoxide and hydrogen using radioactive carbon isotope C^{14}. Dokl Akad Nauk SSSR. 224:1081–1084
19. Studt F, Behrens M, Kunkes EL, Thomas N, Zander S, Tarasov A, Schumann J, Frei E, Varley JB, Abild-Pedersen F, Nørskov JK, Schlögl R (2015) The mechanism of CO and CO_2 hydrogenation to methanol over Cu-based catalysts. ChemCatChem 7:1105–1111. https://doi.org/10.1002/cctc.201500123
20. Lee S, Sardesai A (2005) Liquid phase methanol and dimethyl ether synthesis from syngas. Top Catal 32:197–207. https://doi.org/10.1007/s11244-005-2891-8
21. Sun J, Yang G, Yoneyama Y, Tsubaki N (2014) Catalysis chemistry of dimethyl ether synthesis. ACS Catal 4:3346–3356. https://doi.org/10.1021/cs500967j
22. Ramos FS, De Farias MD, Borges LEP, Monteiro JL, Fraga M, Sousa-Aguiar EF, Appel LG (2005) Role of dehydration catalyst acid properties on one-step DME synthesis over physical mixtures. Catal Today 101:39–44. https://doi.org/10.1016/j.cattod.2004.12.007
23. Venugopal A, Palgunadi J, Deog JK, Joo OS, Shin CH (2009) Dimethyl ether synthesis on the admixed catalysts of Cu–Zn–Al–M (M = Ga, La, Y, Zr) and γ-Al_2O_3: the role of modifier. J Mol Catal A 302:20–27. https://doi.org/10.1016/j.molcata.2008.11.038
24. Baltes C, Vukojević S, Schüth F (2008) Correlations between synthesis, precursor, and catalyst structure and activity of a large set of CuO/ZnO/Al_2O_3 catalysts for methanol synthesis. J Catal 258:334–344. https://doi.org/10.1016/j.jcat.2008.07.004
25. García-trenco A, Martínez A (2012) Direct synthesis of DME from syngas on hybrid CuZnAl/ZSM-5 catalysts: new insights into the role of zeolite acidity. Appl Catal A 411–412:170–179. https://doi.org/10.1016/j.apcata.2011.10.036
26. Ginés MJL, Amadeo N, Laborde M, Apesteguía CR (1995) Activity and structure-sensitivity of the water–gas shift reaction over Cu single bond Zn single bond Al mixed oxide catalysts. Appl Catal A 131:283–296. https://doi.org/10.1016/0926-860X(95)00146-8
27. Kowalik P, Antoniak-Jurak K, Bicki R, Próchniak W, Wiercioch P, Michalska K (2019) The alcohol-modified CuZnAl hydroxycarbonate synthesis as a convenient preparation route of high activity Cu/ZnO/Al_2O_3 catalysts for WGS. Int J Hydrogen Energy 44:913–922. https://doi.org/10.1016/j.ijhydene.2018.11.051
28. Lima SH, Forrester AMS, Palacio LA, Faro AC (2014) Niobia-alumina as methanol dehydration component in mixed catalyst systems for dimethyl ether production from syngas. Appl Catal A 488:19–27. https://doi.org/10.1016/j.apcata.2014.09.022
29. Rocha AS, Aline AM, Lachter ER, Sousa-Aguiar EF, Faro AC (2012) Niobia-modified aluminas prepared by impregnation with niobium peroxo complexes for dimethyl ether production. Catal Today 2012:104–111. https://doi.org/10.1016/j.cattod.2012.02.062
30. Lang Y, Du C, Tang Y, Chen Y, Zhao Y, Chen R, Liu X, Shan B (2020) Highly efficient copper–manganese oxide catalysts with abundant surface vacancies for low-temperature water-gas shift reaction. Int J Hydrogen Energy 45:8629–8639. https://doi.org/10.1016/j.ijhydene.2020.01.108
31. Tanaka Y, Utaka T, Kikuchi R, Takeguchi T, Sasaki K, Eguchi K (2003) Water gas shift reaction for the reformed fuels over Cu/MnO catalysts prepared via spinel-type oxide. J Catal 215:271–278. https://doi.org/10.1016/S0021-9517(03)00024-1
32. Qi G, Fei J, Zheng X, Hou Z (2001) DME synthesis from CO/H_2 over Cu–Mn/Ă-Al_2O_3 catalyst. React Kinet Catal Lett 73:245–256. https://doi.org/10.1023/A:1014194804329
33. Palgunadi J, Yati I, Jung KD (2010) Catalytic activity of Cu–Zn–Al–Mn admixed with gamma-alumina for the synthesis of DME from syngas: manganese effect or just method of preparation? React Kinet Mech Catal 101:117–128. https://doi.org/10.1007/s11144-010-0205-z
34. Tan Y, Xie H, Cui H, Han Y, Zhong B (2005) Modification of Cu-based methanol synthesis catalyst for dimethyl ether synthesis from syngas in slurry phase. Catal Today. 104:25–29. https://doi.org/10.1016/j.cattod.2005.03.033
35. Tang Q, Huang X, Chen Y, Liu T, Yang Y (2009) Characterization and catalytic application of highly dispersed manganese oxides supported on activated carbon. J Mol Catal A 301:24–30. https://doi.org/10.1016/j.molcata.2008.11.003
36. Ghosh SK (2020) Diversity in the family of manganese oxides at the nanoscale: from fundamentals to applications. ACS Omega 5:25493–25504. https://doi.org/10.1021/acsomega.0c03455
37. Holse C, Elkjær CF, Nierhoff A, Sehested J, Chorkendorff I, Helveg S, Nielsen JH (2015) Dynamic behavior of CuZn nanoparticles under oxidizing and reducing conditions. J Phys Chem C 119:2804–2812. https://doi.org/10.1021/jp510015v

38. Šťastný M, Issa G, Popelková D, Ederer J, Kormunda M, Kříženecká S, Henych J (2021) Nanostructured manganese oxides as highly active catalysts for enhanced hydrolysis of bis(4-nitrophenyl) phosphate and catalytic decomposition of methanol. Catal Sci Technol 11:1766–1779. https://doi.org/10.1039/d0cy02112a
39. Zhang QC, Liu ZW, Zhu XH, Wen LX, Zhu QF, Guo K, Chen JF (2015) Application of micro-impinging stream reactors in the preparation of $CuO/ZnO/Al_2O_3$ catalysts for methanol synthesis. Ind Eng Chem Res 54:8874–8882. https://doi.org/10.1021/acs.iecr.5b01775
40. Nijs H, Jacobs PA (1980) New evidence for the mechanism of the Fischer–Tropsch synthesis of hydrocarbons. J Catal 411:401–411. https://doi.org/10.1016/0021-9517(80)90043-3
41. Andersson MP, Remediakis IN, Bligaard T, Jones G, Lytken O, Horch S, Nielsen JH, Sehested J, Chorkendorff I (2008) Structure sensitivity of the methanation reaction: H_2-induced CO dissociation on nickel surfaces. J Catal 255:6–19. https://doi.org/10.1016/j.jcat.2007.12.016